Liquid Sulfur Impregnation of Microporous Carbon Accelerated by Nanoscale Interfacial Effects

Tod A. Pascal,*[†] Irune Villaluenga,[‡,⊥] Kevin H. Wujcik,[‡,§] Didier Devaux,[‡,⊥] Xi Jiang,[§] Dunyang Rita Wang,[§,‖] Nitash Balsara,[‡,§,⊥] and David Prendergast*[†]

[†]Molecular Foundry, Lawrence Berkeley National Laboratory, Berkeley, California 94720, United States
[‡]Department of Chemical and Biomolecular Engineering, University of California, Berkeley, California 94720, United States
[§]Materials Sciences Division, Lawrence Berkeley National Laboratory, Berkeley, California 94720, United States
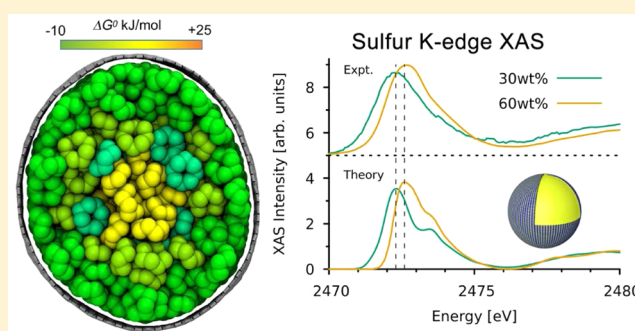[‖]Department of Materials Science and Engineering, University of California, Berkeley, California 94720, United States
[⊥]Energy Technologies Area, Lawrence Berkeley National Laboratory, Berkeley, California 94720, United States

S Supporting Information

ABSTRACT: Impregnation of porous carbon matrices with liquid sulfur has been exploited to fabricate composite cathodes for lithium−sulfur batteries, aimed at confining soluble sulfur species near conducting carbon to prevent both loss of active material into the electrolyte and parasitic reactions at the lithium metal anode. Here, through extensive computer simulations, we uncover the strongly favorable interfacial free energy between liquid sulfur and graphitic surfaces that underlies this phenomenon. Previously unexplored curvature-dependent enhancements are shown to favor the filling of smaller pores first and effect a quasi-liquid sulfur phase in microporous domains (diameters <2 nm) that persists ∼30°

below the expected freezing point. Evidence of interfacial sulfur on carbon is shown to be a 0.3 eV red shift in the simulated and measured interfacial X-ray absorption spectra. Our results elucidate the critical morphology and thermodynamic properties necessary for future cathode design and highlight the importance of molecular-scale details in defining emergent properties of functional nanoscale interfaces.

KEYWORDS: Battery, energy storage, sulfur, spectroscopy, nanoscale, computer simulation, molecular dynamics, free energy, entropy

The need for advanced renewable energy storage materials, brought on by heightened concerns about the economic and environmental cost of the continued combustion of fossil fuels, has renewed interest in battery technologies[1] for storage of iterant renewable energy sources. Most promising is lithium−sulfur (LiS) batteries,[2] owing to the affordability and availability of sulfur, their lightweight and high theoretical capacity (1675 mAh/g), and energy density (2600 Wh/kg), both of which exceed the performance of traditional lithium ion batteries (LIBs) by a factor of ∼5. Indeed, unlike intercalation-based LIBs, discharge of LiS batteries operate based on chemical interconversion of octa-sulfur (S_8) to lithium sulfide (Li_2S) at the cathode, according to the basic reaction

$$16Li^+ + 16e^- + S_8 \rightarrow 8Li_2S \qquad (1)$$

Equation 1 is of course oversimplified and masks intermediate reactions that form broken chain sulfur species[3,4] (termed lithium polysulfides). The chemistry of these polysulfides with chain lengths (x) that vary from 2 to 8, is complicated by various interconversion and/or disproportionation reactions[5−7] that may result in distributions of dianions (Li_2S_x) or radicals (LiS_x) species in solution.[6,8−12] Fundamental

to the poor cyclability and capacity fading of LiS batteries then is the dissolution of polysulfides into the electrolyte[13] and out of electrical contact with the cathode. Eventual parasitic reactions at the anode lead to battery failure.

Methods of confining sulfur within the cathode thus continue to be of intense interest. Fabrication of cathodes based on highly porous, graphitic materials has emerged as a promising avenue,[14] because graphitic carbon is electrically conductive and already constitutes an essential additive, given that both sulfur and lithium sulfide are insulators. Spatial confinement in carbon nanoshells[15−19] is a more recent advance aimed at maximizing sulfur loading within the shell interiors while simultaneously confining species due to the microporosity of the shell walls. The assumption is that micro- or mesoporous carbon are sufficient to (1) permit the entry of molten (or sublimed) sulfur when fabricating cathodes and electrolyte during operation but (2) prevent or significantly hinder the escape of polysulfides based on size[20] or unfavorable chemical interactions.[21]
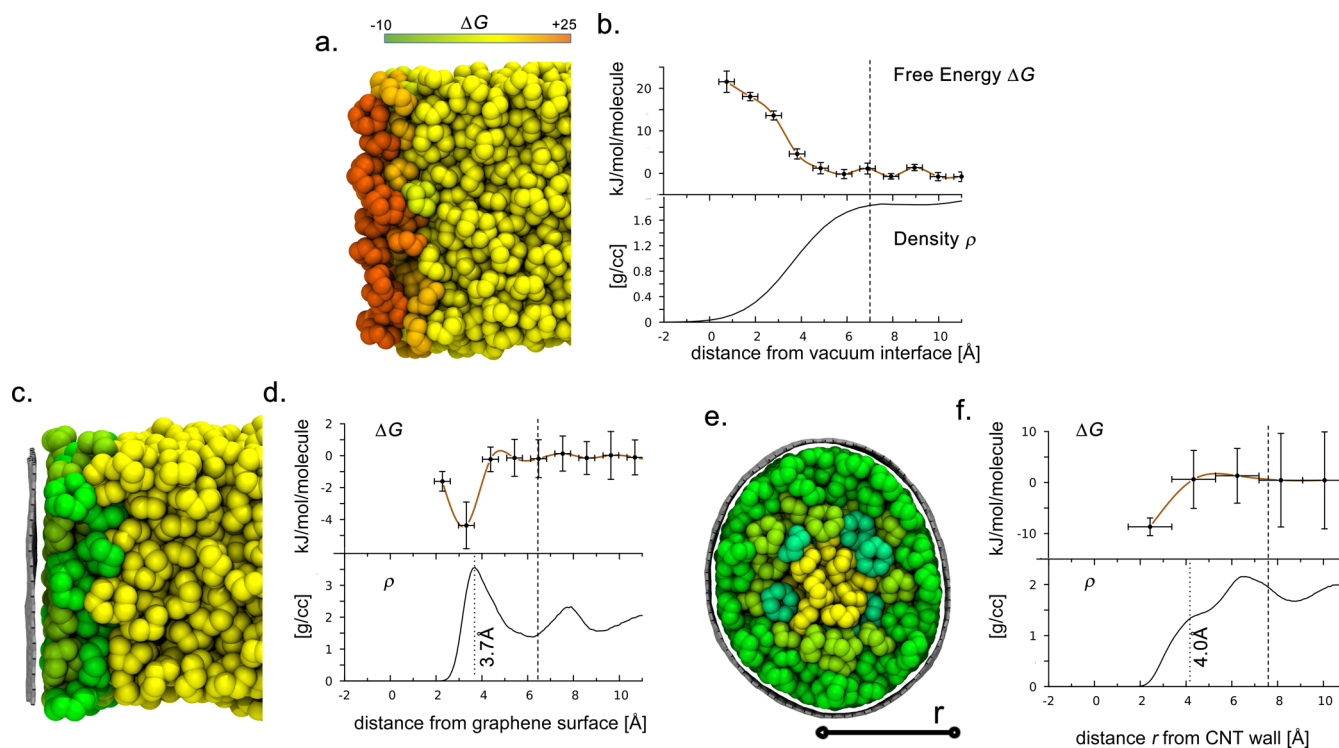
Figure 1. Structure and thermodynamics of liquid sulfur at T_m = 390 K from CMD simulations. (a) Representative snapshot of sulfur at the vacuum interface. Sulfur molecules are colored based on their relative stability compared to the bulk (see colorbar inset) (b) Top panel: Profile of relative Gibbs free energy per molecule. The calculated values (points) are connected with a cubic spline (gold line) for presentation purposes. Vertical dashed line demarcates the interfacial from bulk sulfur molecules and represents the convergence point in the free energy. Bottom panel: Sulfur density profile. Left dotted line represents the position of the first peak maximum (c) Snapshot of the graphene/liquid sulfur interface. The carbon atoms (silver) are shown. (d) Free energy and density profiles at the sulfur/graphene interface. The graphene sheet (not shown) is centered at 0. (e) Snapshot of equilibrium structure of sulfur molecules encapsulated in a 5 nm diameter CNT. (f) Free energy and density profile of sulfur as a function of distance from the CNT walls.

Maximizing the performance of porous carbon/sulfur composite cathodes depends on a nanoscale appreciation of which regions naturally favor sulfur accumulation and whether this is of benefit to electrochemical function. This in turn demands selective probes of the buried functional interface with nanometer resolution in order to reveal molecular details of critical energy conversion processes. Modern characterization techniques, such as microscopy and scattering methods, are limited in their abilities to extract such spatial distributions, however, due primarily to the ease with which sulfur can sublime under vacuum conditions and the coincidence in density of the two materials. Indeed, small-angle X-ray scattering has exploited this fact recently[22] to deduce the length scales of biphasic domains, indicating that sulfur might (as has often been postulated) selectively fill microporous regions first. In this contribution, we advance a combined theoretical and experimental approach that elucidates the thermodynamic underpinning of melt impregnation and develop a universal model for predicting this phenomenon based solely on the surface free energies. Thus, we sample thermodynamic ensemble structures and simulate X-ray absorption (XAS) spectra that are revealed here to be a robust probe of sulfur molecules within 2 nm of the carbon walls. This prediction is validated by our own surface sensitive XAS measurements on loaded carbon nanospheres, and the selective filling of the microporous shells is evident in electron microscopy images employing chemical contrast via energy dispersive X-ray spectroscopy (EDS).

Results and Discussion. Our investigations are based initially on equilibrium, classical molecular dynamics (CMD) simulations of model systems comprising various width carbon nanotube capillaries in contact with liquid octa-sulfur (S_8) reservoirs. Our simulation methodology is detailed in the methods section of Supporting Information. Briefly, all simulations were performed at temperatures above the sulfur melting point (T_m = 390 K) but below the polymerization temperature (430 K), leveraging highly optimized analytic potentials to describe the sulfur[23] and graphene[24] self-interactions. We developed our own force field for describing the critical carbon−sulfur interactions by fitting to binding curves from density functional theory calculations employing a self-consistent van der Waals functional (vdw-DF2)[25] (Figure S1 and Table S1). We chose a Buckingham potential $E = Ae^{-r/\rho} - \frac{C}{r^6}$ to describe the energy E as a function of distance r, with A = 1.5 × 10^5 kJ/mol, ρ = 0.325/Å, C = 4880 Å^6 kJ/mol. As a figure of merit, we calculate a binding energy of an isolated sulfur molecule to a graphene sheet of −64 kJ/mol (~−660 meV), about half the heat of sublimation of crystalline sulfur at room temperature (−102.4 kJ/mol from this work vs −99.71 kJ/mol from experiments[26]). At equilibrium, the center of mass of an isolated sulfur molecule sits ~4.0 Å above the flat graphene plane.

Figure 1 shows the profile of the sulfur free energy per molecule as a function of distance from the vacuum and graphene interfaces, and inside a 5 nm radius carbon nanopore (depicted in Figure S2). We find that liquid sulfur molecules at
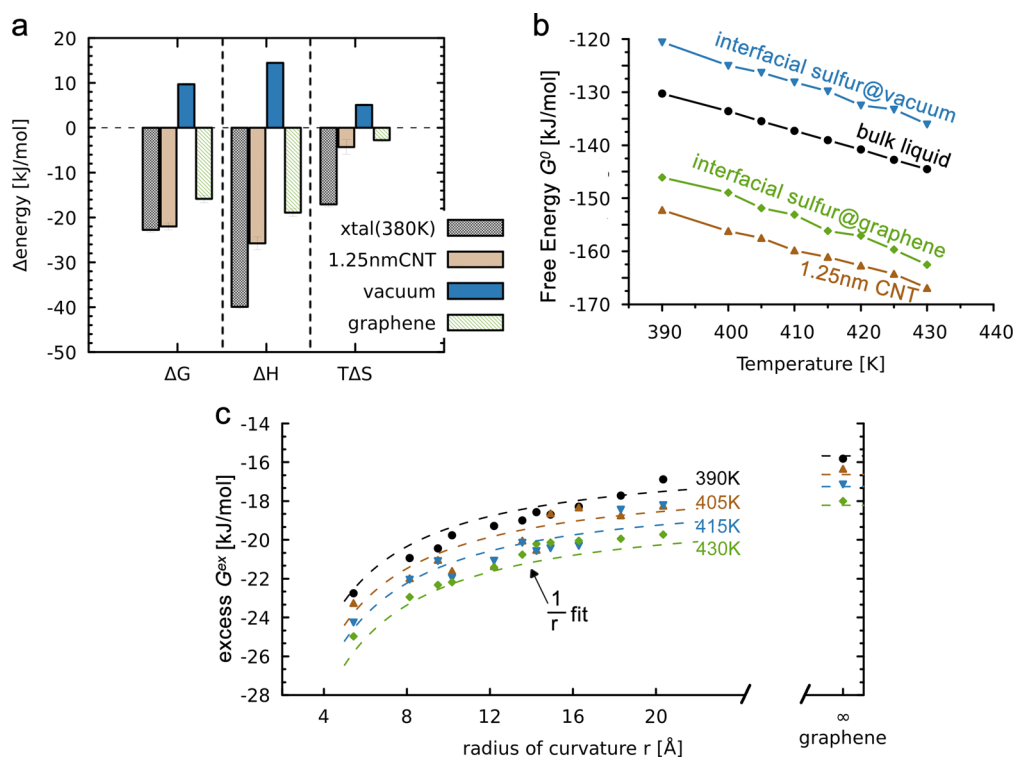
Figure 2. Temperature-dependent equilibrium thermodynamics of sulfur. (a) Sulfur thermodynamics at the melting temperature T_m = 390 K. The excess Gibbs free energy G^{ex}, enthalpy H^{ex}, and entropy TS^{ex} of the sulfur molecules encapsulated in nanopores and at the vacuum and graphene interfaces are presented. The thermodynamics of the crystalline α-S_8 at 380 K is given as reference. (b) Per molecule Gibbs free energy of bulk liquid sulfur (black), interfacial sulfur at the vacuum interface (blue), interfacial sulfur on graphene (green), and encapsulated in a 1.25 nm diameter CNT (gold). (c) Relative per molecule excess sulfur interfacial free energy versus radius of curvature r. The dashed line is a plot of eq 4. The predicted and calculated value for a flat graphene sheet is provided for reference.

the vacuum interface are less stable than in the bulk at T_m with ΔG = +9.7 kJ/mol/molecule (~101 meV, see Table S2 for details). Here, losses in intermolecular binding overcome gains in entropy, resulting in a free energy cost for forming the interface γ_{LV} (that is, the surface tension) of 56.2 mJ/m^2 (dyn/cm), which is in good agreement with experimental estimates.[27] In contrast, sulfur molecules at the graphene interface have more stable free energies compared to the bulk liquid, that is, ΔG = −15.8 kJ/mol/molecule (~164 meV). Favorable sulfur−graphene interactions stabilize the enthalpy and overcompensate entropic losses arising from densification and suppressed intermolecular librations at the interface. The net result is a calculated liquid/solid surface energy γ_{SL} of −41.9 mJ/m^2. Note that unlike the liquid−vapor surface tension, there is no experimental measurement that can directly access the solid/liquid surface tension. It can however be obtained indirectly, through Young's equation[28]

$$\gamma_{LV} \cos \Theta = \gamma_{SV} - \gamma_{SL} \qquad (2)$$

which relates the measured contact angle Θ to the surface tensions. Applying eq 2 and assuming a negligible solid/vapor surface tension γ_{SV} = 0, we calculate a 41.8° ± 6.9° contact angle for sulfur on graphene at T_m (Table S3), which increases to 46.2° ± 11.2° for graphite (modeled as six layer graphene), again in reasonable agreement with recent experiments.[29]

The increased stability of liquid sulfur at the planar graphene interface, compared to the vacuum interface, leads naturally to the observed wetting (low contact angle) behavior. Furthermore, one would expect that the favorable interfacial free energy would drive liquid sulfur into pores with aspect ratios

(length versus radius) smaller than that predetermined by the contact angle Θ [a spherical cap droplet of height h has a width $a = h \sin \Theta/(1-\cos \Theta)$]. However, we find that sulfur molecules in microporous carbon capillaries have even lower free energies per molecule than just the interfacial region next to a graphene sheet. This is evident from our equilibrium CMD simulations, where the initially evacuated nanopores spontaneously fill with sulfur within 10 ps, displaying Langmuir-like filling kinetics; after an initial barrier, associated with overcoming the liquid/vapor surface energy, individual sulfur molecules diffuse into the nanopores and coalesce to eventually fill the pores (Figure S2c).

We note that the spontaneous filling of microporous carbon with sulfur is somewhat counterintuitive, given that the filled pores comprise both a thin interfacial layer and a bulk-like interior with less favorable free energy per molecule than the flat interface. We obtain clues as to the physical origin of the implied nanoscale stabilization forces from structural analysis, which shows that the impregnated sulfur molecules exist as a mixed phase: the molecules are highly diffusive, as in the liquid (Figure S3), but are also quite ordered, as in the solid. We denote this as a quasi-liquid phase. In fact, the first interfacial sulfur layer is preferentially oriented in-plane with the nanopore axis (Figure S4), maximizing sulfur−carbon contact. At the planar graphene interface, the first interfacial molecular layer is located (on average) 3.7 Å from the surface, closer than the optimal 4.0 Å separation of an isolated molecule. This is a reflection of both the softness and long-range of the sulfur−carbon interaction in this geometry, where sulfur molecules in adjacent layers are also attracted to the carbon walls, pushing
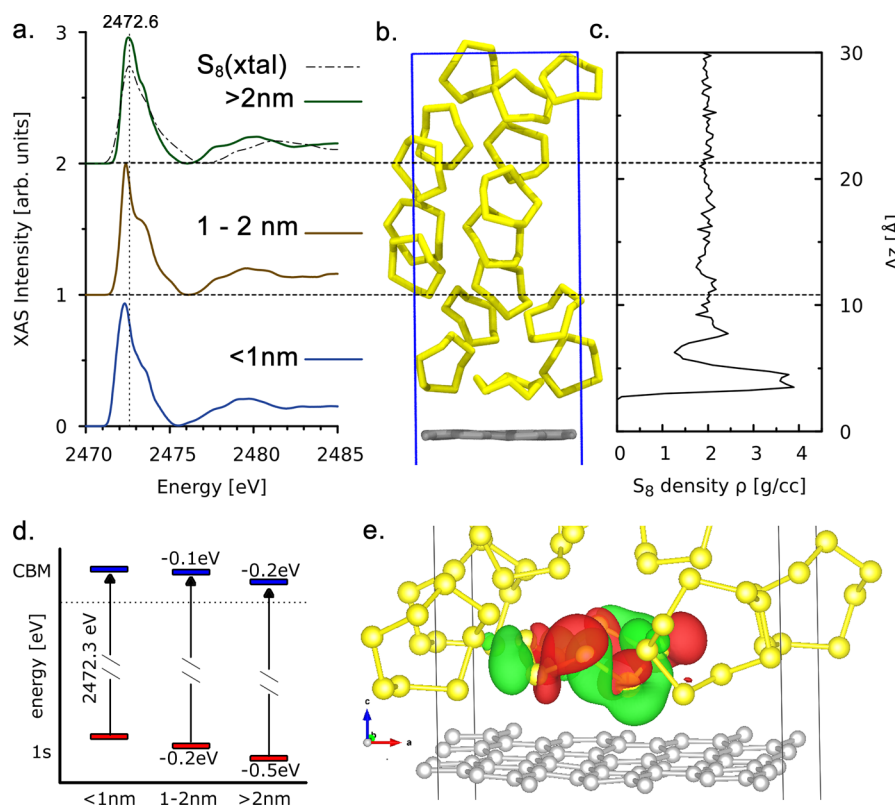
Figure 3. Electronic structure of sulfur near graphene. (a) (from top to bottom) Calculated XCH K-edge X-ray absorption spectra of sulfur molecules >2 nm (green), 1−2 nm (brown), and <1 nm (blue) from the graphene interface. The vertical dashed line is the bulk sulfur "white line" at 2472.6 eV. The XAS of liquid sulfur at 415 K is given as reference (dash-dot). (b) Snapshot of the simulation cell, showing the sulfur atoms (yellow) and the carbon plane. (c) Density of sulfur (molecular center of mass) as a function of distance from the graphene sheet from FPMD simulations. (d) Energy level diagram showing the shifts in 1s core (red) and conduction band minimum (CBM, blue). The data (bars) is averaged over all sulfur atoms within the indicated range and the height of the bar indicates the standard deviation. (e) Electron orbital of the core excited state of an interfacial sulfur molecule. The excited atom is indicated with a cross. The positive (red) and negative (green) phases of the orbital are shown.

the interfacial molecules closer. However, for the somewhat rigid S_8 ring molecules inside pores with nanoscale radii of curvature, the closest approach of the molecular center of mass is limited by the shortest carbon−sulfur atomic distances at the ring perimeter, constraining some sulfur atoms to be more distant from the surface and leading to average carbon−sulfur separations closer to the optimal 4.0 Å. Figure 2a shows that this slight extension in carbon−sulfur separation leads to a 4−8 kJ/mol/molecule increased stabilization in the interfacial free energy of the impregnated sulfur molecules, compared to the flat interface.

As shown in Figure 2b, the nanoscale stabilization of impregnated sulfur persists over the entire temperature range of the liquid. Additionally, we find that the quasi-liquid impregnated sulfur molecules remain in thermodynamic equilibrium with the crystalline solid down to 360 K within a 1.25 nm diameter nanopore (Figure S5), representing a 30 K depression of the melting point.[30] For a liquid confined in cylindrical pores of radius r, the Gibbs−Thomson equation[31] describes the depression of the melting temperature, $\Delta T_m = T_{m,bulk} − T_{m,pore}$, of encapsulated molecules in terms of the surface energies[30] as follows

$$\Delta T_m = \frac{T_{m,bulk}(\gamma_{SS} − \gamma_{SL})\nu}{r\lambda_{bulk}} \qquad (3)$$

where γ_{SS} is the solid−solid (i.e., graphene−solid sulfur) interfacial free energy, calculated to be −30.2 mJ/m² from our

simulations. Taking a calculated molar volume ν of 15.4 cm³/mol/atom and a calculated λ_{bulk}, the latent heat of melting, of 5 kJ/mol/atom, eq 3 leads to a calculated depression in the melting temperature of 22.5 K for a 1.25 nm diameter nanopore. Note that using the actual surface free energy of the 1.25 nm tube of −46.23 mJ/m² leads to a predicted ΔT_m of 30.8 K, which is in very close agreement with the estimate from our MD simulations, and suggests deviation from the macroscopic Gibbs−Thomson equation due to specific molecular interactions at the nanoscale. We also note that the depression of the melting point of nanoencapsulated sulfur is opposite to the recently observed melting point enhancement ($\Delta T_m < 0$) for water encapsulated in carbon nanotubes[32]

The relative stability of interfacial sulfur molecules decreases with increasing nanopore size, as expected from the geometric arguments cited above, and the overall thermodynamics of the system can be partitioned into adsorbed molecular layers with lower average free energy, and a bulk phase beyond ∼1 nm from the interface. This suggests a scaling law to predict excess interfacial free energy of sulfur molecules in filled carbon nanopores *a priori*. We use two terms: a constant referring to sulfur molecules at the flat graphene interface (i.e., zero curvature) and a geometric term (which should scale like the inverse pore radius) and fit the excess free energies of impregnated sulfur molecules in microporous carbon at T_m to

$$\Delta G^{ex}(r) = G_{nanopore}(r) − G_{bulk}(r) = \frac{\alpha}{r} + \beta \qquad (4)$$
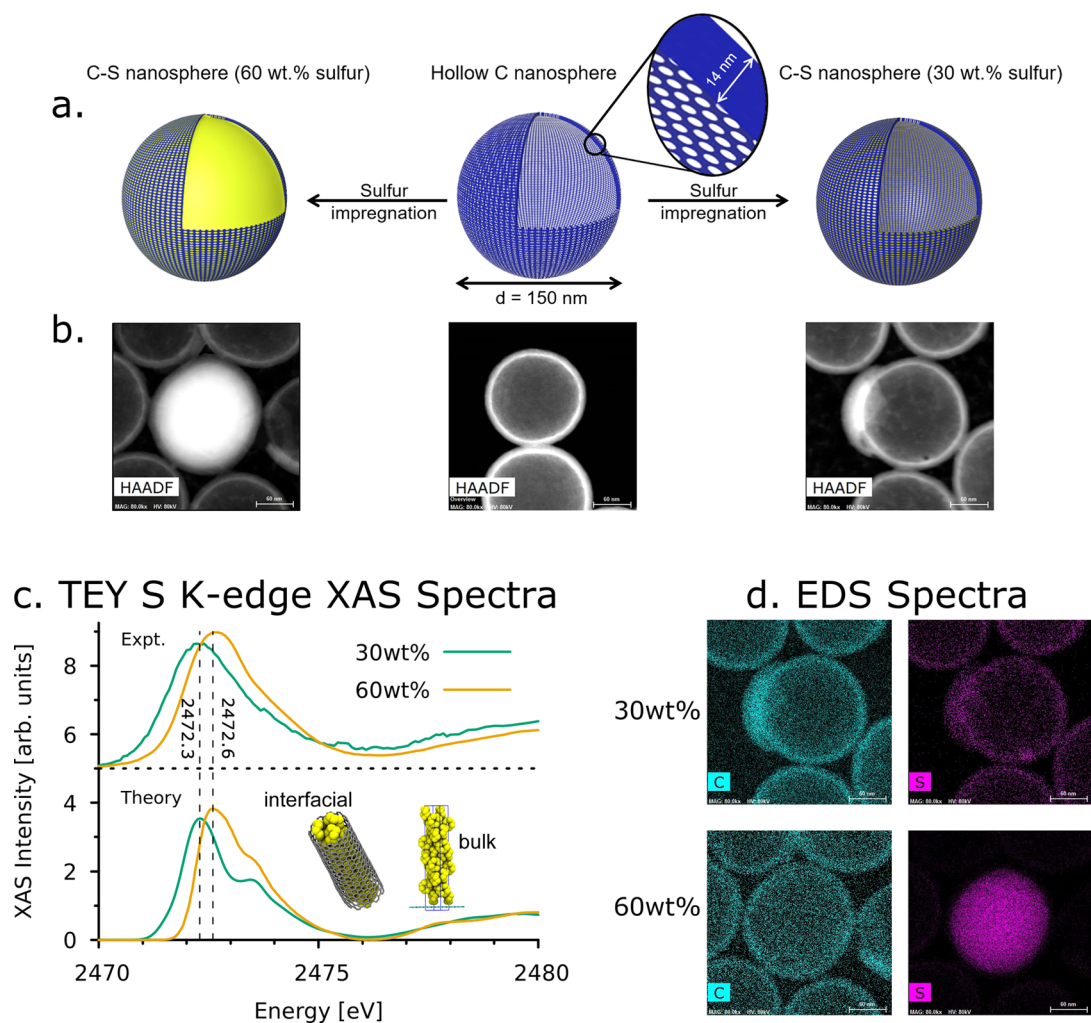
Figure 4. Structure of C−S nanospheres. (a) Schematic of the 60 wt % (left) and 30 wt % (right) carbon nanosphere morphology (b) associated high-angle annular dark-field (HAADF) images. (c) Simulated (XCH, bottom) and measured (total electron yield, top) X-ray absorption spectra of 30 wt % (green) and 60 wt % (brown) loaded carbon nanoshells. Dashed vertical lines indicate the positions of peak maximum. Bottom insets: Models used when calculating the XAS of the 30 and 60 wt % nanoshells, respectively. (d) Energy dispersive X-ray spectra of nanoshells at the carbon and sulfur edges.

which results in $\alpha = -37.4$ kJ Å/mol and $\beta = -15.7$ kJ/mol. The limiting constant β correctly approaches the asymptotic limit of interfacial sulfur molecules on graphene calculated from our MD simulations: $\Delta G^{ex} = -15.8$ kJ/mol. α defines the curvature dependent, nanoscale parameter for sulfur/carbon, which being negative leads to increasingly stable sulfur molecules with smaller pore radius. We note that for more strongly interacting liquids, the parameters α and β may have opposite signs, which would then preclude their spontaneous impregnation into microporous regions or nanotubes, as has been observed for some liquids.[33]

Our thermodynamic model predicts the free energy of sulfur molecules in larger diameter nanopores (not included in the fit) to within 2% of the value calculated from MD simulations at T_m. It can also be straightforwardly extended to account for the temperature dependent filling. Considering the Gibbs equation, $\Delta G^{ex} = \Delta H^{ex} - T\Delta S^{ex}$, we write

$$\Delta G^{ex}(r, T) = \Delta H^{ex}(r) - T\Delta S^{ex}(r) = \frac{a}{r} + b - T\left(\frac{c}{r} + d\right)$$

(5)

which leads to a set of universal scaling constants, $a = -1.2$ kJ Å/mol and $b = 9.3$ kJ/mol, the enthalpic nanoscale and limiting terms respectively, and $c = 93$ J Å/mol/K and $d = 64$ J/mol/K, the respective entropic terms. As shown in Figure 2c, eq 5 predicts the free energy of sulfur encapsulated in various sized nanopores, as well as at the graphene interface, to within 3% of the values calculated from MD simulations over the entire liquid temperature range (Figure S6).

As with our previous efforts,[34,35] we aim to uncover electronic structure changes upon sulfur impregnation into microporous carbon that can be exploited to both resolve the underlying physical morphologies and reveal molecular scale details of function. A previous study demonstrated that surface molecules at metal interfaces have unique electronic structure, manifested as modulations of their X-ray absorption spectra (XAS).[36] We reveal an analogous effect in Figure 3, where our simulated XAS show that sulfur molecules within the first 1 nm of the graphene interface present a main-edge peak at 2472.3 eV, that is 0.3 eV lower in energy than the bulk sulfur peak at 2472.6 eV (the so-called "white line"). Similarly, sulfur molecules within 1−2 nm of the interface have a main peak that is red-shifted by ∼0.1 eV, while the XAS of molecules 2 nm

or more beyond the graphene interface resemble the bulk crystalline phase. The XAS red shift in the interfacial sulfur has two causes: a reduced 1s core−electron binding and a depressed energy for the first available orbital to accept electrons (analogous to the lowest unoccupied molecular orbital) for molecules near the graphene (Figure 3d), both due to additional (semimetallic) screening by the delocalized valence electron cloud on graphene. The resulting interfacial core-excited states are localized on the individual sulfur molecules (Figure 3e) with a small amount of hybridization with the graphene electronic structure and a slight reduction in the peak intensity relative to the crystalline molecular solid.[36]

XAS measurements on microporous carbon nanoshells (Figure 4a) impregnated with 30 and 60 wt % liquid sulfur by melt diffusion at 428 K are used to validate our predictions. BET analysis of the empty nanoshells revealed pore sizes ranging from 1−1.3 nm (Figure S7) and TEM imaging confirmed the incorporation of sulfur into the carbon nanoshell structure (Figure 4b). We note that the sulfur loadings were chosen so that if sulfur preferentially impregnated the micropores, the 30 wt % sample would constitute completely filled pores, while the 60 wt % sample would contain significant amounts of bulk sulfur in the remaining free volume. In support of this hypothesis, room-temperature X-ray diffraction measurements revealed the presence of crystalline sulfur in the 60 wt % sample, but only amorphous sulfur in the 30 wt % sample (Figure S8). Figure 4c compares the interface sensitive XAS of interfacial sulfur in the carbon nanopores at various sulfur loadings. The measurements were obtained in total electron yield mode, by measuring the drain current which neutralizes photoionization and Auger decay events. Our XAS simulations effectively modeled the spectrum of the 30 wt % sample using a 1.2 nm diameter carbon nanotube completely filled with sulfur molecules and the 60 wt % sample using 5 nm of crystalline sulfur resting on graphene (Figure S9). We obtained excellent agreement in the peak positions and line shapes for the two sulfur loadings from both theory and experiments. This favorable comparison is proof that at 30 wt % only the microporous regions are filled with sulfur. Additional sulfur resides in pores of diameter significantly larger than 2 nm, which, as we show, can provide a bulk-like spectrum, and permit crystallization. Finally, spatially resolved, high-resolution EDS measurements showed evidence of sulfur near the pore walls of the nanoshells in the 30 wt % sample with little or no evidence of sulfur in the interior void (Figure 4c). Conversely, the EDS of the 60 wt % sample showed evidence of sulfur everywhere.

In this work, we only considered pure carbon surfaces, absent of any surface functional groups that might be present.[15] We see no spectroscopic evidence for a significant amount of oxidized sulfur that might result from chemical interactions with reactive moieties, and so even if oxygen is present (Figure S10) we imagine it to be mostly unreactive and interacting with sulfur molecules in a manner similar to the carbon surface: repulsive at short-range and attractive through weak van der Waals forces at longer distances. This reality is therefore not expected to change the underlying conclusions of our simplified model except perhaps through some roughening of the surfaces.

In summary, we have shown that liquid sulfur will preferentially and spontaneously impregnate microporous carbon, accelerated by nanoscale curvature and the quasi-rigid ring geometry of the S_8 molecules. The melting temperature of the resulting diffusive interfacial phase is depressed by 30 K with respect to the bulk liquid. We also predicted that sulfur molecules within 2 nm of the graphene interface should display a red-shifted X-ray absorption peak. The preference to fill microporous regions first and the corresponding spectral signature are validated by measured XAS spectra for sulfur-impregnated microporous carbon nanospheres. More generally, we have demonstrated how a combination of computer simulations, incorporating finite temperature effects, and electronic structure calculations can be used to interpret complex experimental measurements and reveal new physics of functional nanoscale interfaces. We chose to focus on the initial loading of porous carbons with sulfur in matrices with porosity distributions on at least two distinct length scales with nanospheres boasting both mesoporous interiors and microporous shell walls. We leave investigations of the functioning sulfur cathode and other material interfaces to future work.

ASSOCIATED CONTENT

ⓢ Supporting Information

The Supporting Information is available free of charge on the ACS Publications website at DOI: 10.1021/acs.nanolett.7b00249.

Theoretical and experimental methods, Tables S1−S5 and Figure S1−S10 (PDF)

AUTHOR INFORMATION

Corresponding Authors
*E-mail: (T.A.P.) tapascal@lbl.gov.
*E-mail: (D.P.) dgprendergast@lbl.gov.

ORCID
Tod A. Pascal: 0000-0003-2096-1143
Irune Villaluenga: 0000-0002-1299-2479
Nitash Balsara: 0000-0002-0106-5565

Author Contributions
The manuscript was written through contributions of all authors. All authors have given approval to the final version of the manuscript.

Notes
The authors declare no competing financial interest.

■ REFERENCES

(1) David, H.; Pat, D.; Dane, B.; Dave, D.; Linda, H.; John, V. U.S. Department of Energy Vehicle Battery R&D: Current Scope and Future Directions. U.S. Department of Energy. http://energy.gov/sites/prod/files/Battery_SEAB_Presentation_1-31-12.pdf (accessed on 01/21/2014).

(2) Peramunage, D.; Licht, S. *Science* **1993**, *261*, 1029−1032.

(3) Kumaresan, K.; Mikhaylik, Y.; White, R. E. *J. Electrochem. Soc.* **2008**, *155*, A576−A582.

(4) Akridge, J. R.; Mikhaylik, Y. V.; White, N. *Solid State Ionics* **2004**, *175*, 243−245.

(5) Yamin, H.; Gorenshtein, A.; Penciner, J.; Sternberg, Y.; Peled, E. *J. Electrochem. Soc.* **1988**, *135*, 1045−1048.

(6) Barchasz, C.; Molton, F.; Duboc, C.; Leprêtre, J.-C.; Patoux, S.; Alloin, F. *Anal. Chem.* **2012**, *84*, 3973−3980.

(7) Patel, M. U.; Demir-Cakan, R.; Morcrette, M.; Tarascon, J. M.; Gaberscek, M.; Dominko, R. *ChemSusChem* **2013**, *6*, 1177.

(8) Nazar, L.; Cuisinier, M.; Cabelguen, P.-E.; Adams, B.; Garsuch, A.; Balasubramanian, M. *Energy Environ. Sci.* **2014**, *7*, 2697.

(9) Patel, M. U.; Demir-Cakan, R.; Morcrette, M.; Tarascon, J. M.; Gaberscek, M.; Dominko, R. *ChemSusChem* **2013**, *6*, 1177−1181.

(10) Wang, H.; Yang, Y.; Liang, Y.; Robinson, J. T.; Li, Y.; Jackson, A.; Cui, Y.; Dai, H. *Nano Lett.* **2011**, *11*, 2644−2647.

(11) Cuisinier, M.; Cabelguen, P.-E.; Evers, S.; He, G.; Kolbeck, M.; Garsuch, A.; Bolin, T.; Balasubramanian, M.; Nazar, L. F. *J. Phys. Chem. Lett.* **2013**, *4*, 3227−3232.

(12) Wujcik, K. H.; Pascal, T. A.; Pemmaraju, C.; Devaux, D.; Stolte, W. C.; Balsara, N. P.; Prendergast, D. *Adv. Energy Mater.* **2015**, *5*, 1500285.

(13) Mikhaylik, Y. V.; Akridge, J. R. *J. Electrochem. Soc.* **2004**, *151*, A1969−A1976.

(14) Wang, D.-W.; Zeng, Q.; Zhou, G.; Yin, L.; Li, F.; Cheng, H.-M.; Gentle, I. R.; Lu, G. Q. M. *J. Mater. Chem. A* **2013**, *1*, 9382−9394.

(15) Ji, X.; Lee, K. T.; Nazar, L. F. *Nat. Mater.* **2009**, *8*, 500−506.

(16) Ji, L.; Rao, M.; Zheng, H.; Zhang, L.; Li, Y.; Duan, W.; Guo, J.; Cairns, E. J.; Zhang, Y. *J. Am. Chem. Soc.* **2011**, *133*, 18522−18525.

(17) Seh, Z. W.; Li, W.; Cha, J. J.; Zheng, G.; Yang, Y.; McDowell, M. T.; Hsu, P.-C.; Cui, Y. *Nat. Commun.* **2013**, *4*, 1331.

(18) Li, W.; Zheng, G.; Yang, Y.; Seh, Z. W.; Liu, N.; Cui, Y. *Proc. Natl. Acad. Sci. U. S. A.* **2013**, *110*, 7148−7153.

(19) Liang, C.; Dudney, N. J.; Howe, J. Y. *Chem. Mater.* **2009**, *21*, 4724−4730.

(20) Li, C.; Ward, A. L.; Doris, S. E.; Pascal, T. A.; Prendergast, D.; Helms, B. A. *Nano Lett.* **2015**, *15*, 5724−5729.

(21) Villaluenga, I.; Wujcik, K. H.; Tong, W.; Devaux, D.; Wong, D. H.; DeSimone, J. M.; Balsara, N. P. *Proc. Natl. Acad. Sci. U. S. A.* **2016**, *113*, 52−57.

(22) Petzold, A.; Juhl, A.; Scholz, J.; Ufer, B.; Goerigk, G.; Fröba, M.; Ballauff, M.; Mascotto, S. *Langmuir* **2016**, *32*, 2780−2786.

(23) Ballone, P.; Jones, R. O. *J. Chem. Phys.* **2003**, *119*, 8704−8715.

(24) Pascal, T. A.; Karasawa, N.; Goddard, W. A., 3rd *J. Chem. Phys.* **2010**, *133*, 134114.

(25) Lee, K.; Murray, E. D.; Kong, L.; Lundqvist, B. I.; Langreth, D. C. *Phys. Rev. B: Condens. Matter Mater. Phys.* **2010**, *82*, 081101.

(26) Meyer, B. *Chem. Rev.* **1976**, *76*, 367−388.

(27) Fanelli, R. *J. Am. Chem. Soc.* **1950**, *72*, 4016−4018.

(28) Young, T. *Philos. Trans. R. Soc. London* **1805**, *95*, 65−87.

(29) Kaban, I.; Nowak, R.; Bruzda, G.; Xi, L.; Sobczak, N.; Eckert, J.; Giebeler, L. *Carbon* **2016**, *98*, 702−707.

(30) Sliwinska-Bartkowiak, M.; Gras, J.; Sikorski, R.; Radhakrishnan, R.; Gelb, L.; Gubbins, K. E. *Langmuir* **1999**, *15*, 6060−6069.

(31) Evans, R.; Marconi, U. M. B. *J. Chem. Phys.* **1987**, *86*, 7138−7148.

(32) Agrawal, K. V.; Shimizu, S.; Drahushuk, L. W.; Kilcoyne, D.; Strano, M. S. *Nat. Nanotechnol.* **2016**, *12*, 267.

(33) Dujardin, E.; Ebbesen, T. W.; Hiura, H.; Tanigaki, K. *Science* **1994**, *265*, 1850−1852.

(34) Pascal, T. A.; Pemmaraju, C. D.; Prendergast, D. *Phys. Chem. Chem. Phys.* **2015**, *17*, 7743−7753.

(35) Pascal, T. A.; Wujcik, K. H.; Velasco-Velez, J.; Wu, C.; Teran, A. A.; Kapilashrami, M.; Cabana, J.; Guo, J.; Salmeron, M.; Balsara, N.; Prendergast, D. *J. Phys. Chem. Lett.* **2014**, *5*, 1547−1551.

(36) Velasco-Velez, J. J.; Wu, C. H.; Pascal, T. A.; Wan, L. W. F.; Guo, J. H.; Prendergast, D.; Salmeron, M. *Science* **2014**, *346*, 831−834.